Mapping the myoglobin concentration, oxygenation, and optical pathlength in heart ex vivo using near-infrared imaging

Gussakovsky, Eugene; Yang, Yanmin; Rendell, John; Jilkina, Olga; Kupriyanov, Valery

Publisher's version / Version de l'éditeur:
https://doi.org/10.1016/j.ab.2010.07.010
Analytical Biochemistry, 407, 1, pp. 120-127, 2010-12-01

Mapping the myoglobin concentration, oxygenation, and optical pathlength in heart ex vivo using near-infrared imaging

Gussakovsky, Eugene; Yang, Yanmin; Rendell, John; Jilkina, Olga; Kupriyanov, Valery

Abstract

A method that provides maps of absolute concentrations of oxygenated and deoxygenated myoglobin (Mb), its oxygenation, and its near-infrared (NIR) optical pathlength in cardiac tissue was developed. These parameters are available simultaneously. The method is based on NIR diffuse reflectance spectroscopic imaging and specific processing of the NIR images, which included a first derivative of the diffuse reflectance spectrum. Mb oxygenation, total Mb concentration, and NIR light pathlength were found to be in the range of 92%, 0.3 mM, and 12.5 mm, respectively, in beating isolated buffer-perfused and arrested pig hearts. The charge-coupled device camera enables sub-millimeter spatial resolution and spectroscopic imaging in 1.5 to 2.0 min. The technique is noninvasive and nondestructive. The equipment has no mechanical contact with the tissue of interest, leaving it undisturbed.

Keywords: Myoglobin; NIR light diffuse reflectance; NIR spectroscopic imaging; First derivative; Optical pathlength; Pig heart

Article Outline

The mapping of subepicardial hemoglobin (Hb)[1] + myoglobin (Mb) oxygenation in pig hearts has been reported using a near-infrared (NIR) spectroscopic imaging technique that, however, does not provide absolute concentrations and is limited to the oxygen saturation parameter (OSP) only [1], [2], [3], [4] and [5]. In spite of these limitations, the efficiency of this approach in cardiac research has been shown to be significant [6], [7] and [8]. The technique has used a charge-coupled device (CCD) camera and a narrow-band (7–10 nm) electronically tunable interference filter of chosen wavelengths.

No experimentally determined maps of the absolute Hb and Mb concentrations in cardiac tissue or other muscles at the macroscopic level with resolution in sub-millimeter and millimeter ranges have been reported. A CCD-based spectroscopic imaging technique in the NIR and visible regions, implying high spatial resolution, has been used for brain and skin analysis, including Hb quantification and oxygenation [9], [10], [11] and [12]. These imaging approaches cannot provide the actual optical pathlength.

A method for determination of the absolute concentration of oxygenated and deoxygenated (Hb + Mb) and light pathlength in cardiac ventricular wall employing the first derivative of diffuse reflectance spectra recorded at selected points with a fiber-optic technique has been reported [13] and [14]. On this basis, it became possible to employ this approach for NIRSI data and obtain the maps of absolute (Hb + Mb) concentration, OSP, and light pathlength simultaneously.

The absorption spectra of Hb and Mb, either oxygenated or deoxygenated, in the NIR region are shifted by approximately 4 to 5 nm [15], [16] and [17], which does not allow their spectroscopic separation when the spectral resolution is worse than 4 nm. In addition, the Hb content in hearts is variable depending on the blood volume, pressure, and hematocrit (relative red blood cell volume), whereas Mb content is constant for the heart tissue. The current article shows how the approach developed for the fiber-optic technique can be realized for the NIR imaging of buffer-perfused pig hearts and heart tissue samples when Mb is the only heme protein significantly contributing to the diffuse reflectance in the NIR region.

Materials and methods

Diffuse reflectance imaging

Three halogen lamps with reflectors homogeneously illuminated the pig heart or pig heart slices at approximately 25 to 30 cm from the tissue surface. The reflector concentrated the light beam in a 24° stereo angle.

Diffuse reflectance imaging was performed with an NIR spectroscopic system that included an infrared-sensitive CCD array camera consisting of a back-illuminated CCD element and a 14/16-bit ST-138 analog-to-digital converter run in 16-bit mode (Photometrics, Tucson, AZ, USA), a Nikon AF-60 microlens and a CRI VariSpec SNIR/NNIR liquid crystal tunable filter (LCTF) (Woburn, MA, USA). Binning (2 × 2) was performed to increase the signal-to-noise ratio and to produce final images of 256 × 256-pixel resolution. The system was assembled and the operating software was developed at NRC Institute for Biodiagnostics (Canada). The camera allows imaging with a frame readout time of 536.8 ms in the wavelength range of 200 to 1100 nm. The LCTF works as an electronically activated tunable interference filter in the range of 650 to 1100 nm with a bandwidth of 7 nm and a response time of 150 ms. LCTF-based spectral imaging principles have been reviewed previously [1], [2], [3] and [18].

Such spectral imaging provided a diffuse reflectance spectrum at each pixel for a total of 65,536 spectra. The diffuse reflectance spectrum at each pixel (x,y) was converted to a pseudo-optical density (POD) spectrum $P_{xy}(\lambda)$ [13] and [14] according to

$$P_{xy}(\lambda) = -\log_{10}\frac{I_{xy}(\lambda)}{I_{0xy}(\lambda)}, \quad (1)$$

where $I_{xy}(\lambda)$ and $I_{0xy}(\lambda)$ are light intensities diffusely reflected from a heart surface and a reference, respectively, acquired in the wavelength range of 650 to 1050 nm with a wavelength increment of 4 nm. White polyurethane sponge was employed as a reference [19] and [20]. The calculations based on the first derivative of the pseudo-optical density spectrum (Eq. (1)), and described in Results and Discussion, were performed for the wavelength range of 700 to 1040 nm.

Absolute Mb concentration, OSP, optical pathlength, and related calculations were performed with a program written using MatLab version 7.1 software (MathWorks, Natick, MA, USA).

Molar extinction coefficient spectra of oxygenated and deoxygenated tetrameric Hb, as well as methemoglobin (metHb) and water absorption coefficient spectra, were taken from Refs. [21],

[22], [23] and [24] and Zijlstra and coworkers [24] (250–1024 nm). Dividing the intensities of these spectra by 4 (number of hemes in the tetrameric hemoglobin molecule) results in the Hb spectra per heme. These spectra were used instead of Mb spectra, not different from the Hb spectra with the resolution of 4 to 5 nm [15], [16] and [17].

The raw diffuse reflectance spectra $I_{xy}(\lambda)$ and $I_{0xy}(\lambda)$ were smoothed employing a Savitzky–Golay approach [25] for a three-point linear function. Then the $P_{xy}(\lambda)$ spectra were calculated according to Eq. (1).

NIR imaging of beating isolated hearts was made possible by capturing an image at each wavelength in the same point in the cardiac cycle. The gating hardware monitored the cardiac cycle using the first derivative of the left ventricular pressure (dLVP/*dt*), which triggered an image acquisition with delay from the moment when dLVP/*dt* reached maximum. As a result, the camera captured the NIR image at a chosen wavelength corresponding to the acquisition time window ($\sim$80 ms, $\sim$10–15% of the entire cycle) during the diastolic phase. In the Supplementary material, video clips (nongated.imaging.wmv and gated.imaging.wmv) captured by the NIR spectroscopic system at 800 nm clearly show that the gating leads to no significant heart movement during the image acquisition.

Statistics

To quantify a goodness of the fit for the measured spectra, a χ^2 criterion [26] and [27] was used for estimating the statistical significance of the difference between the measured and fit spectra. Following Meyer [26], the χ^2 parameter was calculated as

(2) $$\chi^2 = \sum_{i=1}^{n} \frac{[y_i - f_i]^2}{\sigma_i^2},$$ where y_i is a measured spectrum intensity, f_i is its fit value, σ_i is a standard deviation for y_i, and i refers to wavelength. In the spectral imaging studies, i changed from 1 to $n = 86$, which corresponds to the wavelength range from 700 to 1040 nm with an increment of 4 nm. A null hypothesis $y_i = f_i$ is considered to be true if

(3) $$\chi^2 \le \chi_\alpha^2 = \frac{1}{2}(\sqrt{2n-3} + z_{2\alpha})^2.$$ Here a critical χ_α^2 is given for $n > 30$ [27] and [28]. At a significance level of $\alpha = 0.05$, we have $z_{2\alpha} = 1.6$ and $\chi_\alpha^2 = 106.6$ at $n = 86$.

The results in Table 1 for a *selected* region of interest (ROI) in the arrested heart or a single slice are means and related standard deviations obtained by averaging the data calculated for each pixel in the ROI. The *statistics* results for normal tissue obtained for seven beating hearts or multiple slices are mean values and related standard deviations obtained by averaging the mean results over the ROI for each heart or slice.

Table 1. Mb concentration, oxygenation, and optical pathlength in normal tissue of KHB-perfused pig hearts and heart slices determined using NIR spectroscopic imaging.

Parameter	Heart			Slice	
	Selected	**Statistics**	**Biochemical assay**	**Selected**	**Statistics**
OSP (%)	91.7 ± 2.2	92.3 ± 6.2	92.3 ± 0.3, n = 2 [42] and [43]	0	6.9 ± 9.0
[Total Mb] (μM)	395 ± 175	272 ± 62	284 ± 55, n = 5 [42], [44], [45], [48] and [49]	267 ± 22	271 ± 21
[MbO_2] (μM)	361 ± 162	250 ± 55		0	23 ± 37
[deoMb] (μM)	44 ± 29	28 ± 10		267 ± 22	268 ± 22
L (mm)	12.4 ± 2.8	12.6 ± 2.2		6.9 ± 0.6	6.8 ± 0.6
Criterion	$\chi < \chi^2_\alpha$			$\chi < \chi^2_\alpha$	
χ^2	77.8			52.6	
χ^2_α	106.6			106.6	
N	1	14		1	27

Note. Regions of interest (ROI) chosen on the selected heart corresponds to those in Fig. 1. The data are mean values and standard deviations obtained at the averaging over the ROIs. The statistics is based on the gated imaging of seven KHB-perfused hearts ex vivo. On image of each heart, two ROIs related to normal tissue were chosen resulting in 14 ROIs, totally. For selected slice, the ROI corresponds to the normal tissue as shown in Fig. 3. The statistics for slices is based on the totally 27 ROIs chosen in the normal tissue from the apex and base sides of four slices of the same heart. No correction for the water content in the heart tissue was made.

Pig hearts

All pigs (24–26 kg, n = 7) received humane care in compliance with the guidelines of the Canadian Council on Animal Care [29]. For details of a pig heart surgery and cryoinjury, see Ref. [30]. The isolated pig hearts were excised and perfused in isovolumic (Langendorff) mode with a Krebs–Henseleit buffer (KHB: 25 mM $NaHCO_3$, 118 mM NaCl, 4.7 mM KCl, 1.75 mM $CaCl_2$, 1.2 mM $MgSO_4$, 0.5 mM ethylenediaminetetraacetic acid [EDTA], and 11 mM glucose) and 6 g/L bovine serum albumin as described elsewhere [30]. The perfusate was aerated with 95% O_2/5% CO_2 in a membrane oxygenator providing arterial pO2 of 400 to 550 mm Hg and pH 7.35 to 7.45 at 37 °C. Venous pO2 was in the range of 100 to 150 mm Hg, indicating sufficient tissue oxygenation. *S*-Propranolol (beta blocker, 0.5 μM), lidocaine (antiarrythmic drug, 15 μM), and penicillin G (antibiotic, 100,000 U/L) were added to provide stable mechanical function. The function was evaluated as a left ventricular (LV) pressure measured using an intraventricular water-filled balloon connected through rigid plastic tubing to the pressure transducer interfaced with a physiological recorder. The signal in the form of the first derivative of LV pressure (sharper waveform) was fed to a custom-built triggering device that provided a TTL pulse for triggering camera acquisitions (see above). When necessary, contractions of two hearts were

arrested by the addition of KCl to KHB to bring its concentration to 26 mM. In these cases, gating was turned off.

To get 5 to 10-mm-thick slices, the KHB perfusion was terminated, resulting in cessation of mechanical activity. Thereafter, the heart's ventricles were filled with alginate-based cast mixture and the hearts were cut along the short axis using a custom-built slicing device. See Ref. [30] for details. The slice imaging was done within 20 to 25 min after termination of perfusion.

Results and discussion

Theoretical

In general, oxygenated and deoxygenated heme in Hb and Mb, oxidized and reduced cytochrome *c* oxidase, and heme of metHb and/or metmyoglobin (metMb), as well as water and fat, may determine light absorption of cardiac (or other muscle) tissue in the wavelength range (NIR) of 700 to 1050 nm. In this wavelength range, the contribution of cytochrome *c* oxidase to the total light absorption is negligible, as discussed below. Neither metHb nor metMb is capable of oxygen exchange in a biological tissue. Although a metHb/metMb Fe^{3+}-heme extinction coefficient at 700 to 1050 nm is comparable to deoxygenated hemoglobin/deoxygenated myoglobin (deoHb/deoMb) [24], no measurable contribution of metMb to the total diffuse reflectance occurs because the cardiac tissue metMb content is approximately 1% of the total Mb. No Hb remained in the hearts or their slices because of the blood-free KHB perfusion. The contribution of fat is also insignificant (surface layer of <1 mm with a maximal extinction coefficient of $\sim$0.5–1 m^{-1} at 600–900 nm [31] results in absorption of 0.001–0.0005, whereas the Mb absorption in this wavelength range of $\sim$5 mm layer gives an estimate of 0.15–0.25). Therefore, only oxygenated and deoxygenated Mb and water remained under consideration.

Similar to optode-assisted diffuse reflectance spectroscopy [13] and [14], and according to a modified Lambert–Beer law for spectroscopic imaging, the POD spectrum $P_{xy}(\lambda)$ at each pixel (x,y) is

(4) $P_{xy}(\lambda)=[MbO_2]_{xy}\varepsilon_{MbO2}(\lambda)L_{xy}+[deoMb]_{xy}\varepsilon_{deoMb}(\lambda)L_{xy}+\mu_w(\lambda)L_{xy}+s_{xy}(\lambda)+a_o$. Here $[MbO_2]_{xy}$ and $[deoMb]_{xy}$ are concentrations of oxygenated and deoxygenated Mb, respectively, and $\mu_w(\lambda)$ is the light absorption of water per unit of optical pathlength. Extinction coefficients $\varepsilon_{deoMb}(\lambda)$ and $\varepsilon_{MbO2}(\lambda)$ of deoxygenated and oxygenated Mb were considered to be equal to the extinction coefficients of monomeric Hb because neither deoxygenated nor oxygenated Hb or Mb light absorption spectra are distinguishable at a 4-nm resolution. The parameter L_{xy} is an averaged pathlength that reflects the incident light passes through in the cardiac tissue before it comes out of the tissue and is trapped by the CCD camera at each pixel (x,y). It may be thought of as a "banana-shaped" pathlength between the illuminating and light-collecting optodes (a fiber-optic design of the diffuse reflectance measurement) but being a linear combination of the diffuse reflection of various light beams that compose the total homogeneous illumination of the heart surface.

The offset a_o probably reflects the sample-dependent structural inconsistency of the reference and the turbid sample medium as well as, in part, the wavelength-independent contribution of the

reference $\log_{10}(I_o)$. A light-scattering component, $s_{xy}(\lambda)$, at each pixel (x,y) may be described by a power function $\mu_s' = \alpha\lambda^{-n}$ [32], [33] and [34], where $n \sim 1$ according to Refs. [34], [35], [36] and [37]. Using a Taylor series, a first approximation of the $\mu_s'(\lambda)$ may be represented by a linear function of wavelength:

$$\mu_s' L \equiv s_{xy}(\lambda) \approx -\beta_{xy}\lambda. \quad (5)$$

A linear approximation of light scattering in a turbid medium $\mu_s' = a\lambda + b$ has been successfully evaluated previously [32], [38], [39] and [40], and the coefficient at λ was found to be negative [32] as in Eq. (5).

Differentiation of Eq. (4) results in the first derivative $P'_{xy}(\lambda)$ of the POD spectrum of cardiac muscle tissue at each pixel (x,y) in the NIR:

$$P'_{xy}(\lambda) = [\mathrm{MbO_2}]_{xy}\frac{d\varepsilon_{\mathrm{MbO_2}}}{d\lambda} + [\mathrm{deoMb}]_{xy}\frac{d\varepsilon_{\mathrm{deoMb}}}{d\lambda}L_{xy} + \frac{d\mu_w}{d\lambda}L_{xy} - \beta_{xy}, \quad (6)$$

where $d\varepsilon_{\mathrm{deoMb}}/d\lambda$ and $d\varepsilon_{\mathrm{MbO2}}/d\lambda$ are the first derivatives of the deoxygenated and oxygenated Mb extinction coefficients, respectively, and $d\mu_w/d\lambda$ is the first derivative of the light absorption by water.

Restriction of the wavelength range to 700 to 1050 nm eliminates the contribution of chromophores other than MbO_2 and deoMb, such as hemes of metMb and a binuclear Cu_a center of cytochrome *c* oxidase, to the total light absorption in this wavelength range. The negligible contribution of metHb is discussed above. Theoretically, the copper-containing reduced and oxidized cytochrome *c* oxidase could contribute to the NIR diffuse reflectance spectrum, having mean extinction coefficients of 1.7 to 3.3 $\mathrm{mM^{-1}\ cm^{-1}}$ over the range of 700 to 1000 nm (deduced from Ref. [23]). However, the contribution should be negligible because the content of this enzyme in heart (14 μM protein [41]) is approximately 5% of the Mb content (0.3 mM) (Table 1) with similar extinction coefficients of 1.8–2.5 $\mathrm{mM^{-1}\ cm^{-1}}$ [23]. Therefore, neither metHb nor cytochrome *c* oxidase was taken into account in Eq. (6).

Similar to the procedure described in Refs. [13] and [14], if the molar extinction coefficients of the two forms of Mb and water are known, Eq. (6) may be considered as a linear combination of four components, $[\mathrm{MbO_2}]_{xy} \times L_{xy}$, $[\mathrm{deoMb}]_{xy} \times L_{xy}$, L_{xy}, and β_{xy}, with related factors for each pixel (x,y). When $P'_{xy}(\lambda)$ is an *n*-component vector column $\mathbf{P}_{xy}$ (*n* is the number of wavelengths λ taken in the $P'(\lambda)$ spectrum), Eq. (6) becomes a system of linear equations of rank 4 with regard to four unknowns, $[\mathrm{MbO_2}]_{xy} \times L_{xy}$, $[\mathrm{deoMb}]_{xy} \times L_{xy}$, L_{xy}, and β_{xy}, with the matrix of

$$\mathbf{M} = (\varepsilon'_{MbO_2}; \varepsilon'_{deoMb}; \mu'_s; \mathbf{E}), \quad (7)$$

where ε'_{MbO_2}, ε'_{deoMb}, and μ'_s are vector columns of *n* elements representing the first derivatives $d\varepsilon_{\mathrm{MbO2}}/d\lambda$, $d\varepsilon_{\mathrm{deoMb}}/d\lambda$, and $d\mu_w/d\lambda$, respectively, at *n* wavelengths. Vector column **E** consists of *n* ones. Accordingly, matrix **M** has four columns and *n* rows. Obviously, the matrix **M** is the same for each pixel (x,y).

The unknowns form a vector column $\Xi_{xy} = \{\xi_{1xy}, \xi_{2xy}, \xi_{3xy}, \xi_{4xy}\}$ of four elements: $\xi_{1xy} = [\mathrm{MbO_2}]_{xy} \times L_{xy}$, $\xi_{2xy} = [\mathrm{deoMb}]_{xy} \times L_{xy}$, $\xi_{3xy} = L_{xy}$, and $\xi_{4xy} = \beta_{xy}$. Then Eq. (6) in a matrix form is

(8)$\mathbf{P}_{xy}=\mathbf{M}\otimes\underline{\Xi}_{xy}$, where $\otimes$ denotes matrix multiplication. The solution of this equation gives all unknowns, ξ_{1xy}, ξ_{2xy}, ξ_{3xy}, and ξ_{4xy}, from which absolute concentrations of MbO_2 and deoMb can be deduced easily as $[MbO_2]_{xy} = \xi_{1xy}/\xi_{3xy}$ and $[deoMb]_{xy} = \xi_{2xy}/\xi_{3xy}$. Thus, the solution delivers the absolute concentrations of deoxygenated and oxygenated Mb and the actual averaged light pathlength L as well as the "scattering" factor β at each pixel (x,y).

In practice, the MatLab software function *lsqnonneg* uses matrix **M** and vector $\mathbf{P}_{xy}$ in Eq. (8) and provides the best least squares solution for Ξ_{xy} with a constraint that all unknowns are positive. Once this solution is performed for each pixel (x,y), the matrices $[MbO_2]_{xy}$, $[deoMb]_{xy}$, L_{xy}, and β_{xy} represent maps of concentrations of oxygenated and deoxygenated Mb, optical pathlength, and the light scattering factor determined independent of each other.

OSP is an additional parameter important for characterization of the heart status. It is defined as the ratio of oxygenated Mb to total Mb and can be easily calculated when the concentrations of deoxygenated and oxygenated Mb are determined for each pixel (x,y):

$$\mathrm{OSP}_{xy} = \frac{[\mathrm{MbO_2}]_{xy}}{[\mathrm{MbO_2}]_{xy} + [\mathrm{deoMb}]_{xy}}. \quad (9)$$

Once $[MbO_2]_{xy}$ and $[deoMb]_{xy}$ are found, an OSP_{xy} map becomes available from Eq. (9) at each pixel (x,y).

Mapping the isolated perfused heart

The proposed approach provides the determination of maps related to the distribution of concentrations of deoxygenated, oxygenated, and total Mb concentrations, OSP, and optical pathlength L across the subepicardial heart tissue. Fig. 1 shows such maps as well as a raw image captured at 814 nm for a representative arrested pig heart. On the raw image (Fig. 1A), small bright areas cannot be used for analysis because they contain a significant contribution of specular reflectance in addition to the diffuse reflectance.

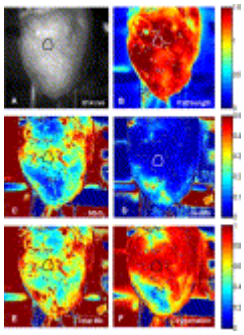

Fig. 1.

Images of an arrested pig heart: (A) raw image captured at 814 nm; (B) map of actual optical pathlength (range = 0–1.5 cm); (C) map of oxygenated Mb concentration (range = 0–0.5 mM);

(D) map of deoxygenated Mb concentration (range = 0–0.5 mM); (E) map of total Mb concentration (range = 0–0.5 mM); (F) map of oxygen saturation parameter (OSP, range = 0–1). In all panels, solid curves indicate ROIs chosen for normal heart tissue as described in the text.

Among all of the maps in Fig. 1, the map of OSP (Fig. 1F) was chosen for the determination of the ROI as delivering the most important information about heart tissue oxygenation. Obviously, the ROI determination is a matter of experimental choice. The chosen ROI depicts normal tissue of the left ventricle. A large area of low OSP (10–30%) in the bottom part of the map relates to a cryoinjured part of the left ventricle. We did not consider it because our previous data [30] suggested little Mb in such scar tissue.

After the ROI is chosen, the program calculates the mean values of all parameters mentioned above (Table 1). Because of the gating during the NIR spectroscopic imaging (see Materials and methods), the beating heart movement is eliminated in the images (e.g., see gated.imaging.wmv video clip in Supplementary material). In this way, maps similar to the arrested heart were obtained for KHB-perfused beating hearts ex vivo. This allowed one to consider the KHB-perfused beating and arrested hearts as a single group of seven hearts.

Once similar ROIs were chosen for all hearts in the group, the parameters calculated for each heart were averaged and are shown in Table 1 as *statistics*. Statistical data do not differ from the data for the selected heart, as a Student's *t* test indicated (the difference is insignificant with $P > 0.05$ for all parameters in the table). Oxygenation (OSP) was maximal and close to 92%, which is consistent with previous data for pig and guinea pig hearts [42] and [43]. Nearly the whole heart surface was well oxygenated, excluding the cryoinjured area. The total Mb concentration was at a level not statistically different from the values determined previously by biochemical approaches.

For either arrested or beating hearts, the $P_{xy}(\lambda)$ data obtained according to Eq. (1) and then numerically differentiated (left part of Eq. (6)) for each pixel (x,y) were averaged over the ROI. The NIR spectroscopic imaging data in Table 1 provide parameters for the right-hand side of Eq. (6), which is a fit of the experimentally obtained averaged differential spectra in the ROI shown in Fig. 2A.

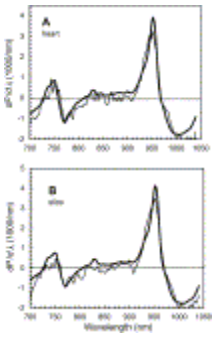

Fig. 2.

First derivative of pseudo-optical density (thin curves) averaged over ROI on surface of arrested pig heart (A) and heart slice (B). The ROIs are from [Fig. 1] and [Fig. 3], respectively. Bold curves show their fits obtained using Eq. (6) and values from Table 1 for selected heart or slice.

When plotted together, the fits were found to be very close to the experimental spectra regarding both the band position and their intensities for the selected heart. To quantify this closeness, a goodness-to-fit χ^2 parameter and related criterion (see Materials and methods and Eq. (3)) were applied. As Table 1 shows, the criterion is valid for the selected heart. The fit spectroscopically guarantees the correctness of the calculation results because biochemical Mb quantification approaches are based on the spectrophotometric measurements [42], [44] and [45].

Mapping the heart slices

The whole heart imaging probed the surface of the hearts, which includes both subepicardium and deeper myocardium layers (depth of NIR light penetration of $\sim$3–5 mm [46] and [47]). In contrast to the whole heart, the NIR spectroscopic imaging of slices can be performed for the transmural myocardium without any contribution from the epicardium.

An alginate-based cast mixture shown as the blue material on a regular color photograph (Fig. 3A) allowed preservation of the heart slice geometry as it is in the isolated heart. The cast mixture occupies mostly the left and right ventricles. Most of the slice tissue represents the entire left ventricle wall thickness where the ROI refers to a normal area.

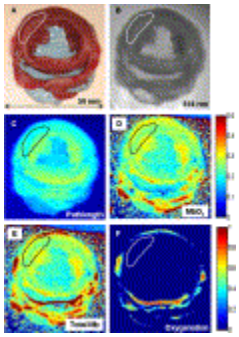

Fig. 3.

Images of slice (base-faced side) taken from a middle part of a pig heart after KHB perfusion (see Materials and methods for details): (A) color photograph of the slice; (B) raw image captured at 814 nm; (C) map of actual optical pathlength (range = 0–1 cm); (D) map of deoxygenated Mb concentration (range = 0–0.5 mM); (E) map of total Mb concentration

(range = 0–1 mM); (F) map of oxygen saturation parameter (OSP, range = 0–1). Panel A shows an actual size scale. In all panels, solid curves indicate ROIs chosen for normal myocardium as described in the text. (For interpretation of the reference to color in this figure legend, the reader is referred to the Web version of this article.)

The CCD camera, lens, and LCTF were deliberately adjusted to artificially defocus the image. This allowed testing the effect of the defocusing on the mapping. The raw image captured at 814 nm (Fig. 3B) illustrates such defocusing. The maps of optical pathlength (Fig. 3C), oxygenated Mb concentration (Fig. 3D), total Mb concentration (Fig. 3E), and OSP (Fig. 3F) were obtained as described in the "Theoretical" section above and in a similar way as for the whole heart. Fig. 3A to 3F show the chosen ROI over which the calculated values of Mb, OSP, and L were averaged and compiled in Table 1.

The fit of the first derivative spectra of NIR spectral images averaged over the ROI related to normal myocardium (Fig. 2B) met the criterion given (Eq. (3) and Table 1). Therefore, the calculations based on these spectra were correct.

OSP was zero over the entire surface of the slice, excluding the edge areas where optical effects can occur. We cannot exclude the possibility that the epicardial tissue also contributes to the high OSP values. Total and oxygenated Mb concentrations as well as optical pathlength were distributed heterogeneously across the left ventricle wall thickness. The low sharpness of the optical pathlength map at the slice edge correlates with that of the 814-nm raw image and is probably caused by the lack of focus.

Whole hearts versus heart slices

In general, the mapping results obtained for the whole hearts should be consistent with the data for the heart slices. However, comparison of the Mb concentration in the deoxygenated and oxygenated states is impossible because in the KHB-perfused heart the buffer regulates the oxygenation state, whereas in slices the Mb deoxygenation is predictable.

Nevertheless, the total Mb concentration does not depend on the Mb oxygenation, so the comparison is valid. Table 1 shows that when statistical [total Mb] corresponded to normal tissue in whole hearts (272 ± 62 μM, $n = 14$) and in heart slices (271 ± 21 μM, $n = 27$), the Student's t test resulted in no difference between them with $P > 0.05$. These values are also consistent with the Mb concentration biochemically found in pig, bovine, and dog hearts (284 ± 55 μM, $n = 5$ [42], [44], [45], [48] and [49], $P > 0.05$ for both whole hearts and heart slices). A similar correspondence occurs for oxygenation of Mb in the hearts [42] and [43].

Spatial resolution

Two factors limit the spatial resolution in the absence of sample movement: CCD camera resolution and camera lens focusing. The CCD camera provided imaging with a resolution of 256 × 256 pixels (see Materials and methods). Under our conditions, 256 linear pixels

corresponded to 100 ± 1 mm for the heart imaging and to 50 ± 1 mm for the slice imaging. Hence, the camera-dependent limitation of the NIRSI was 100/256 ~ 0.4 mm/pixel or 0.16 mm^2/pixel for hearts and approximately 0.2 mm/pixel or 0.04 mm^2/pixel for slices.

In the raw 814-nm image of the whole heart (Fig. 1A), the background and the heart body can be distinguished with an accuracy of 1 pixel, that is, a 0.4-mm real distance. This determines the sharpness of less than 0.4/50 = 0.008 = 0.8% at the heart size of 50 × 90 mm. Therefore, the real spatial resolution of the OSP, Mb concentration, and optical pathlength maps was equal to the camera resolution of 0.4 mm/pixel.

The current imaging of the slice shows an effect of the lens defocusing on the total spatial resolution. A significant defocusing can be seen when a highly sharpened regular color photograph (Fig. 3A) is compared with a raw image at 814 nm (Fig. 3B). On the image, the background and the heart body can be distinguished with an accuracy of 7 pixels related to a 7 × 0.2-mm = 1.4-mm real distance. Therefore, OSP, Mb concentration, and optical pathlength maps had the resolution of 1.4 mm.

In this case, the sharpness was approximately 1.4/40 = 0.035 = 3.5% at the slice diameter of approximately 40 mm. This spatial resolution is 4.4 times lower than that for the heart imaging at the 0.8% sharpness. Obviously, the lens defocusing limits the map resolution at a given CCD camera resolution.

A spatial resolution of 0.45 mm has been achieved by applying spectral imaging in the visible region but without quantifying the absolute concentration of heme proteins and oxygenation using a device built for perfusion imaging of hand palms [12]. Other NIR imaging systems based on the application of multiple optodes provide spatial resolution in the range of 4 to 40 mm (see, e.g., Refs. [48], [49], [50], [51], [52] and [53]), which is one to two orders of magnitude lower than in our measurements.

Acknowledgments

This work was supported in part by a Manitoba Health Research Council Grant for V.K. Contributions of the National Research Council of Canada Institute of Biodiagnostics surgical staff (A. Turner, S. Germscheid, L. Gregorash, and R. Mariash) are acknowledged and greatly appreciated.

References

[1] S.P. Nighswander-Rempel, R.A. Shaw, J.R. Mansfield, M. Hewko, V.V. Kupriyanov and H.H. Mantsch, Regional variations in myocardial tissue oxygenation mapped by near-infrared spectroscopic imaging, *J. Mol. Cell. Cardiol.* **34** (2002), pp. 1195–1203.

[2] S.P. Nighswander-Rempel, R.A. Shaw, V.V. Kupriyanov, J. Rendell, B. Xiang and H.H. Mantsch, Mapping tissue oxygenation in the beating heart with near-infrared spectroscopic imaging, *Vib. Spectrosc.* **32** (2003), pp. 85–94.

[3] S.P. Nighswander-Rempel, V.V. Kupriyanov and R.A. Shaw, Relative contributions of hemoglobin and myoglobin to near-infrared spectroscopic images of cardiac tissue, *Appl. Spectrosc.* **59** (2005), pp. 190–193

[4] M.G. Sowa, J.R. Mansfield, G.B. Scarth and H.H. Mantsch, Noninvasive assessment of regional and temporal variations in tissue oxygenation by near-infrared spectroscopy and imaging, *Appl. Spectrosc.* **51** (1997), pp. 143–152.

[5] R.A. Shaw, J.R. Mansfield, V.V. Kupriyanov and H.H. Mantsch, In vivo optical near-infrared spectroscopy and imaging of metalloproteins, *J. Inorg. Biochem.* **79** (2000), pp. 285–293.

[6] V.V. Kupriyanov, D.M. Manley and B. Xiang, Detection of moderate regional ischemia in pig hearts in vivo by near-infrared and thermal imaging: effects of dipyridamole, *Int. J. Cardiovasc. Imaging* **24** (2008), pp. 113–123.

[7] D.M. Manley, B. Xiang and V.V. Kupriyanov, Visualization and grading of regional ischemia in pigs in vivo using near-infrared and thermal imaging, *Can. J. Physiol. Pharmacol.* **85** (2007), pp. 382–395.

[8] V.V. Kupriyanov, S.P. Nighswander-Rempel and B. Xiang, Mapping regional oxygenation and flow in pig hearts in vivo using near-infrared spectroscopic imaging, *J. Mol. Cell. Cardiol.* **37** (2004), pp. 947–957.

[9] A.K. Dunn, A. Devor, H. Bolay, M.L. Andermann, M.A. Moskowitz, A.M. Dale and D.A. Boas, Simultaneous imaging of total cerebral haemoglobin concentration, oxygenation, and blood flow during functional activation, *Opt. Lett.* **28** (2003), pp. 28–30.

[10] A. Vogel, V.V. Chernomordik, J.D. Riley, F. Amyot, B. Dasgeb, S.G. Demos, R. Pursley, R.F. Little, R. Yarchoan, Y. Tao and A.H. Gandjbakhche, Using noninvasive multispectral imaging to quantitatively assess tissue vasculature, *J. Biomed. Opt.* **12** (2007), p. 051604.

[11] K.J. Zuzak, M.D. Schaeberle, M.T. Gladwin, R.O. Cannon and I.W. Levin, Noninvasive determination of spatially resolved and time-resolved tissue perfusion in humans during nitric oxide inhibition and inhalation by use of a visible-reflectance hyperspectral imaging technique, *Circulation* **104** (2001), pp. 2905–2910.

[12] K.J. Zuzak, M.D. Schaeberle, E.N. Lewis and I.W. Levin, Visible reflectance hyperspectral imaging: characterization of a noninvasive in vivo system for determining tissue perfusion, *Anal. Chem.* **74** (2002), pp. 2021–2028.

[13] E. Gussakovsky, O. Jilkina, Y. Yang and V.V. Kupriyanov, Hemoglobin plus myoglobin concentrations and NIR light pathlength in phantom and pig hearts determined by diffuse reflectance spectroscopy, *Anal. Biochem.* **382** (2008), pp. 107–115.

[14] E. Gussakovsky, O. Jilkina, Y. Yang and V.V. Kupriyanov, Non-invasive measurements of hemoglobin + myoglobin, their oxygenation, and NIR light pathlength in heart in vivo by diffuse reflectance spectroscopy, *Proc. SPIE* **7161** (2009) 71612L1–71612L2.

[15] D.J. Marcinek, C.E. Amara, K. Matz, K.E. Conley and K.A. Schenkman, Wavelength shift analysis: a simple method to determine the contribution of hemoglobin and myoglobin to in vivo optical spectra, *Appl. Spectrosc.* **61** (2007), pp. 665–669.

[16] K.A. Schenkman, D.R. Marble, E.O. Feigl and D.H. Burns, Near-infrared spectroscopic measurement of myoglobin oxygen saturation in the presence of hemoglobin using partial least-squares analysis, *Appl. Spectrosc.* **53** (1999), pp. 325–331.

[17] L.S.L. Arakaki and D.H. Burns, Multispectral analysis for quantitative measurements of myoglobin oxygen fractional saturation in the presence of hemoglobin interference, *Appl. Spectrosc.* **46** (1992), pp. 1919–1928.

[18] K. Burton, J. Jeong, S. Wachsmann-Hogiu and D.L. Farkas, Spectral optical imaging in biology and medicine. In: J.G. Fujimoto and D.L. Farkas, Editors, *Biomedical Optical Imaging*, Oxford University Press, New York (2009), pp. 29–72.

[19] E.E. Gussakovsky and V.V. Kupriyanov, Assessment of infra-red path length in fibrous phantom and muscle tissue, *Appl. Spectrosc.* **62** (2008), pp. 671–676.

[20] M.L. Vernon, J. Frechette, Y. Painchaud, S. Caron and P. Beaudry, Fabrication and characterization of a solid polyurethane phantom for optical imaging through scattering media, *Appl. Optics* **38** (1999), pp. 4247–4251.

[21] S.J. Matcher, C.E. Elwell, C.E. Cooper, M. Cope and D.T. Delpy, Performance comparison of several published tissue near-infrared spectroscopy algorithms, *Anal. Biochem.* **227** (1995), pp. 54–68.

[22] S.J. Matcher, M. Cope and D.T. Delpy, Use of the water absorption spectrum to quantify tissue chromophore concentration changes in near-infrared spectroscopy, *Phys. Med. Biol.* **39** (1994), pp. 177–196

[23] http://www.ucl.ac.uk/medphys/research/borl/intro/spectra.

[24] W.G. Zijlstra, A. Buursma and O.W. van Assendelft, *Visible and Near Infrared Absorption Spectra of Human and Animal Haemoglobin: Determination and Application*, VSP, Utrecht, Netherlands (2000).

[25] A. Savitzky and M.J.E. Golay, Smoothing and differentiation of data by simplified least square procedures, *Anal. Chem.* **35** (1964), pp. 1627–1639.

[26] S.L. Meyer, Data Analysis from Scientists and Engineers, John Wiley, New York (1975).

[27] G.A. Korn, Mathematical Handbook for Scientists and Engineers: Definitions, Theorems, and Formulas for Reference and Review, McGraw-Hill, New York (1961).

[28] I.N. Bronstein and K.A. Semendyaev, Mathematical Handbook for Engineers and University Students, Nauka, Moscow (1981).

[29] Canadian Council on Animal Care, Guide to the Care and Use of Experimental Animals, 2nd ed., Canadian Council on Animal Care, Ottawa, Ontario, Canada, 1993.

[30] Y. Yang, J. Sun, P. Gervai, M.L.H. Gruwel, O. Jilkina, E. Gussakovsky, X. Yang and V.V. Kupriyanov, Characterization of cryoinjury-induced infarction with manganese- and gadolinium-enhanced MRI and optical spectroscopy in pig hearts magnetic resonance imaging, *Magn. Reson. Imaging* **28** (2010), pp. 753–766.

[31] R.L.P. van Veen, H.J.C.M. Sterenborg, A. Pifferi, A. Torricelli, E. Chikoidze and R. Cubeddu, Determination of visible near-IR absorption coefficients of mammalian fat using time- and spatially resolved diffuse reflectance and transmission spectroscopy, *J. Biomed. Opt.* **10** (2005), p. 054004.

[32] S.J. Matcher, M. Cope and D.T. Delpy, In vivo measurements of the wavelength dependence of tissue-scattering coefficients between 760 and 900 nm measured with time-resolved spectroscopy, *Appl. Optics* **36** (1997), pp. 386–396.

[33] J.R. Mourant, T. Fuselier, J. Boyer, T.M. Johnson and I.J. Bigio, Predictions and measurements of scattering and absorption over broad wavelength ranges in tissue phantoms, *Appl. Optics* **36** (1997), pp. 949–957.

[34] R. Graaf, J.G. Aarnoudse, J.R. Zijp, P.M.A. Sloot, F.F.M. Demul, J. Greve and M.H. Koelink, Reduced light-scattering properties for mixtures of spherical particles: a simple approximation derived from Mie calculations, *Appl. Optics* **31** (1992), pp. 1370–1376.

[35] R.M.P. Doornbos, R. Lang, M.C. Aalders, F.W. Cross and H.J.C.M. Sterenborg, The determination of in vivo human tissue optical properties and absolute chromophore concentrations using spatially resolved steady-state diffuse reflectance spectroscopy, *Phys. Med. Biol.* **44** (1999), pp. 967–981.

[36] F. Bevilacqua, A.J. Berger, A.E. Cerussi, D. Jakubowski and B.J. Tromberg, Broadband absorption spectroscopy in turbid media by combined frequency-domain and steady-state methods, *Appl. Optics* **39** (2000), pp. 6498–6507.

[37] W. Verkruysse, R. Zhang, B. Choi, G. Lucassen, L.O. Svaasand and J.S. Nelson, A library based fitting method for visual reflectance spectroscopy of human skin, *Phys. Med. Biol.* **50** (2005), pp. 57–70.

[38] S.J. Matcher and C.E. Cooper, Absolute quantification of deoxyhaemoglobin concentration in tissue near infrared spectroscopy, *Phys. Med. Biol.* **39** (1994), pp. 1295–1312.

[39] S.J. Matcher, P. Kirkpatrick, K. Nahid, M. Cope and D.T. Delpy, Absolute quantification methods in tissue near infrared spectroscopy, *Proc. SPIE* **2389** (1995), pp. 486–495.

[40] A. Cerussi, N. Shah, D. Hsiang, A. Dunkin, J. Butler and B.J. Tromberg, In vivo absorption scattering and physiologic properties of 58 malignant breast tumors determined by broadband diffuse optical spectroscopy, *J. Biomed. Opt.* **11** (2006), p. 044005.

[41] R.S. Balaban, V.K. Mootha and A. Arai, Spectroscopic determination of cytochrome *c* oxidase content in tissues containing myoglobin or hemoglobin, *Anal. Biochem.* **237** (1996), pp. 274–278.

[42] A.E. Arai, C.E. Kasserra, P.R. Territo, A.H. Gandjbakhche and R.S. Balaban, Myocardial oxygenation in vivo: optical spectroscopy of cytoplasmic myoglobin and mitochondrial cytochromes, *Am. J. Physiol. Heart Circ. Physiol.* **277** (1999), pp. H683–H697.

[43] K.A. Schenkman, D.A. Beard, W.A. Ciesielski and E.O. Feigl, Comparison of buffer and red blood cell perfusion of guinea pig heart oxygenation, *Am. J. Physiol. Circ. Physiol.* **285** (2003), pp. H1819–H1825.

[44] B. Reynafarje, Simplified method for the determination oif myoglobin, *J. Lab. Clin. Med.* **61** (1963), pp. 138–145.

[45] A. Schuder, J.B. Wittenberg, B. Haseltine and B. A Wittenberg, Spectrophotometric determination of myoglobin in cardiac and skeletal muscle: separation from hemoglobin by subunit-exchange chromatography, *Anal. Biochem.* **92** (1979), pp. 473–481.

[46] S.P. Nighswander-Rempel, V. Kupriyanov and R.A. Shaw, Assessment of optical path length in tissue using neodymium and water absorption for application to near-infrared spectroscopy, *J. Biomed. Opt.* **10** (2005), p. 024023.

[47] E. Gussakovsky and Y. Yang, On the emission intensity of fluorescent microspheres in cardiac tissue images, *J. Fluoresc.* **20** (2010), pp. 857–863.

[48] L. Hagler, R.I. Coppes Jr., E.W. Askew, A.L. Hecker and R.H. Herfman, The influence of exercise and diet on myoglobin and metmyoglobin reductase in the rat, *J. Lab. Clin. Med.* **93** (1980), pp. 222–230.

[49] R.F. Coburn, F. Ploegmakers, P. Gondrie and R. Abboud, Myocardial myoglobin oxygen tension, *Am. J. Physiol.* **224** (1973), pp. 870–876.

[50] M. Niwayama, K. Yamamoto, D. Kohata, K. Hirai, N. Kudo, T. Hamaoka, R. Kime and T. Katsumura, A 200-channel imaging system of muscle oxygenation using CW near-infrared spectroscopy, *IEICE Trans. Inf. Syst.* **E85-D** (2002), pp. 115–123.

[51] X. Cheng, J. Mao, R. Bush, D.B. Kopans, R.H. Moore and M. Chorlton, Breast cancer detection by mapping haemoglobin concentration and oxygen saturation, *Appl. Optics* **42** (2003), pp. 6412–6421.

[52] B. Chance, Near-infrared images using continuous, phase-modulated, and pulsed light with quantitation of blood and blood oxygenation, *Ann. N.Y. Acad. Sci.* **838** (1998), pp. 29–45.

[53] K.J. Kek, R. Kibe, M. Niwayama, N. Kudo and K. Yamamoto, Optical imaging instrument for muscle oxygenation based on spatially resolved spectroscopy, *Opt. Exp.* **16** (2008), pp. 18173–18187.